Planar Active Organic Waveguide and Wavelength Filter: Self-Assembled *meso*-Tetratolylporphyrin Hexagonal Nanosheet

Naisa Chandrasekhar, Supratim Basak, Mahamad Ahamad Mohiddon, and Rajadurai Chandrasekar*

Functional Molecular Nano/Micro Solids Laboratory, School of Chemistry, University of Hyderabad, Prof. C. R. Rao Road, GachiBowli, Hyderabad 500 046, India

S *Supporting Information*

ABSTRACT: We have fabricated nearly monodispersed nanocrystalline sheet waveguides from a well−known red emitting *meso*-tetratolylporphyrin molecule (**1**) by following a bottom-up solvent assisted self-assembly technique. The nanosheets thickness is in the range of 110−180 nm. Localized laser illumination showed excitation position dependent exciton polariton (653 and 719 nm) propagation behavior of the sheets. The spatially resolved fluorescence spectra of the sheets showed optical modes at the input and output points, indicating cavity effect. Additionally, because of the reabsorption of the 653 nm emission, the nanosheets also act as wave length filter by cutting off the 653 nm photons from reaching the output end.

KEYWORDS: porphyrins, nanosheet, photonics, organic waveguides, exciton-polariton, optical modes
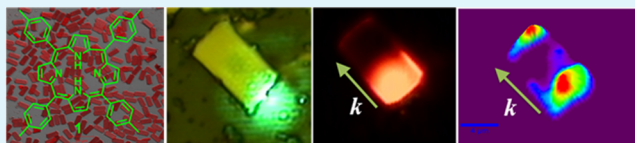
1. INTRODUCTION

Control and manipulation of light within nano/microscale organic optical waveguides (OOW) is one of the raising research areas of organic nanophotonics.[1−14] Compared to silica-based optical waveguides, self-assembled OOWs offer wide range of functionalities, easy processability, flexibility and subwavelength dimensions. Hence these nano/microscale organic materials are one of the prospective components of miniaturized photonic devices. According to physical structure OOWs can also be classified as planar, strip, and fiber waveguides and based on the type of light they propagate OOWs can further be classified into active-[5−14] and passive-[15−20] waveguides. Active wave guides absorb the input laser light and propagates the emitted fluorescence (FL) wave, whereas passive waveguides directly propagates the laser light to the output end.

Recently, we have demonstrated the passive wave guiding behavior of organic submicro tubes, their guiding efficiency and remote sensing properties.[17] Additionally, we have exploited the shape-shifting nature of one dimensional (1D) tubes and two dimensional (2D) sheets to manipulate the light propagation directions.[16] We have also shown the use of Raman spectroscopy as a tool to study the light propagation paths and to detect nano/microscale solid-state defects in the self-assembled organic passive wave guides.[17,18] To control the light propagation distance precisely, we have employed the laser ablation technique as a tool to cut the wave guiding organic tubes.[19] It has also been proposed that in active waveguides, the exciton polariton (EP), which is formed as a result of strong coupling between exciton (correlated electron−hole) and photon (light field) show efficient propagation properties in dielectrics.[21−28] Recently, the active FL wave guiding behavior in the form of propagating EPs in luminescent 1D organic dye fibers and microrings (ring resonators) have

been explored.[5] EPs show extraordinary propagation properties[27] because of low group velocity[28] and subsequent large refractive index[21−23] allowing EPs to move at the wavelength scale in subwavelength scale organic fibers. These properties offer the possibility to construct EP-based miniaturized nanophotonic devices and circuits.

Hence, we intended to explore the active wave guiding behavior of 2D sheets, because the 2D geometry of the sheets confine the light in 1D and allow it to propagate in 2D.[16] Because of planar geometry, the sheet-waveguides are analogues to planar or slab dielectric waveguides. We have used a well-known 5,10,15,20-tetra(*p*-tolyl)porphyrin, also known as *meso*-tetratolylphorphyrin (**1**) as a building block to fabricate nearly monodispersed nano-sheets in THF/water (Figure 1a, inset).[17] Amongst organic π-conjugated systems, porphyrin derivatives are important components in molecular photonic wires, molecular gates, chemosensors, and other molecular electronic and photonic devices.[29] The self-assembly studies of these type photoactive molecules reported in majority of the literature are all mainly based on 1D organic solids such as rods, tubes, wires, belts, etc. However, the study of FL light propagation in 2D porphyrin hexagonal nano-sheet having planar wave guiding geometry is not explored so far. Here for the first time, we report solid state UV-Visible and fluorescence spectroscopy, field emission scanning electron microscopy (FESEM), transmission electron microscopy (TEM), atomic force microscopy (AFM), laser confocal fluorescence microscope (LCFM) and polarised light optical microscopy (PLOM) studies of 2D hexagonal nano-sheets obtained from **1**. We also present the input light dependent
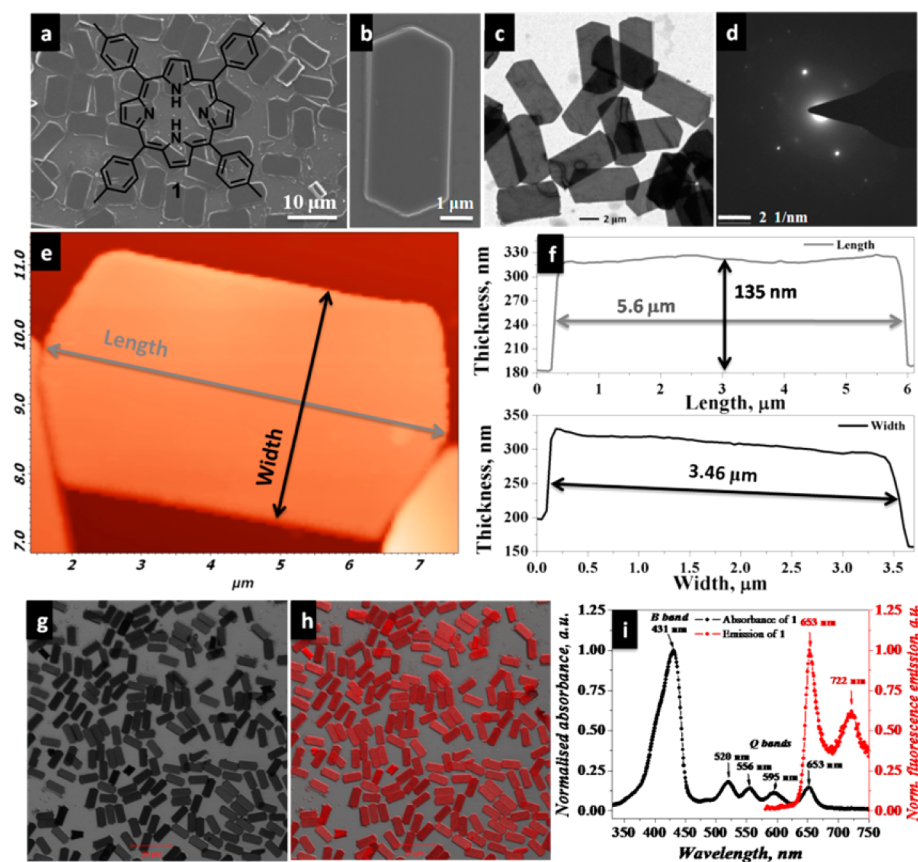
Figure 1. (a) FESEM images of a bunch of nanosheets. Inset shows the chemical structure of compound **1**. (b) FESEM image of a single hexagonal sheet with eight facets. (c) TEM image of nearly monodispersed sheets. (d) Selected area electron diffraction image of a sheet. (e, f) AFM image and profile measurements, respectively displaying length (L), width (W), and thickness (T) of a sheet. (g, h) Bright-field confocal optical microscope image of monodispersed hexagonal sheets without and with 458 nm Ar$^+$ laser excitation, respectively. (i) Solid-state UV−vis absorption and emission spectra of **1**. Black and red lines show the absorption and emission spectra, respectively.

guided fluorescent (FL) light propagation paths in a single nanosheet, between nanosheets, and the tendency of wave guiding nanosheet acting as a wavelength filter.

2. EXPERIMENTAL SECTION

Material and Methods. *Synthesis.* Compound **1** was synthesized as per reported procedure[30] and crystallized in tetrahydrofuran THF or THF/H$_2$O (2:1) solvents. The obtained wine-red color crystals were filtered, air dried and finally used for morphological and active optical waveguiding studies.

Single-Crystal XRD Studies. The single-crystal X-ray data of compound **1** was collected at 298 (2) K on a Bruker Smart Apex CCD area detector system [λ(Mo−Kα) = 0.71073 Å] with a graphite monochromator. The data were reduced using SAINTPLUS, and the structure was solved by using a SHELXS-97 programme and refined using SHELXL-97. The cell parameters obtained from wine-red color crystals of **1** (see the Supporting Information, Table S1) is similar to the reported crystal structure.[30]

Solid-State Absorbance Studies. The solid-state absorbance spectra were collected from a Shimadzu UV-3600 spectrometer in a diffuse reflectance UV−visible (DR−UV−vis) mode. The reflectance spectra were converted to an absorbance spectra using Kubelka-Munk function.

Fabrication of Hexagonal Nanosheets from 1. 1 mg of compound **1** was taken in a test tube and dissolved in 2 ml of tetrahydrofuran (THF). To this was rapidly injected 1 mL of high-purity water (Millipore Milli-Q, resistivity = 18 MΩ cm). Two drops of the sample solution was drop casted on a clean glass slide by using a melting point capillary/μ-syringe for AFM, FESEM, LCFM, and optical waveguiding

studies. Similarly, two drops of the sample solution of **1** was drop-casted on a carbon coated copper grid (200 Mesh) for TEM studies.

Electron Microscopy Studies. Size and morphology of the hexagonal nano-sheets of **1** were examined by using a Carl Zeiss (Model Ultra55) field-emission scaning electron microscope (FESEM) operating at 5 kV. Transmission Electron Microscope (TEM) measurements were performed on a Tecnai G^2 FEI F12 instrument operating at an accelerating voltage of 200 kV. Carbon-coated TEM grids (200 Mesh type-B) were purchased from Ted Pella Inc. USA.

Atomic Force Microscopy Studies. Atomic force microscopy (AFM) was carried out on NT-MDT Model Solver Pro M microscope using a class 2R laser of 650 nm wavelength having maximum output of 1 mW. All calculations and image processing were carried out by using NOVA 1.0.26.1443 software provided by the manufacturer. The images were recorded in a semi-contact mode using a super sharp silicon cantilever (NSG 10_DLC) with a diamond like carbon tip (NT-MDT, Moscow). The dimension of the tip is as follows: cantilever length = 100 (± 5) μm, cantilever width 35 (± 5) μm, and cantilever thickness = 1.7−2.3 μm, resonance frequency = 190−325 kHz, force constant = 5.5−22.5 N/m, chip size = 3.6 × 1.6 × 0.4 mm, reflective side = Au, tip height = 10−20 μm, and DLC tip curvature radius = 1−3 nm.

Laser Confocal Fluorescence Microscope (LCFM) Studies. Confocal fluorescence microscopic images and spectra were recorded on a Carl-Zeiss laser confocal microscopy (Model number NL0710). The emission spectra were recorded in XYλ scan mode, and the fluorescence images collected in XYT mode. 458 nm Argon-ion laser (power- 280 mW) was used as an excitation source (λ = 458 nm).

Polarized Light Optical Microscopic (PLOM) Studies. The polarized light dependent emission behavior of nanosheets was studied on a Nikon eclipse Ti-u inverted microscope. The glass coverslip containing nano-sheets was placed on a sample stage and irradiated with tungsten−halogen lamp source through a bottom water immersion 100× objective lens (NA = 1.10). The rotational polarizer was situated between the light source and the sample. The interacted polarized light coming from the sample was recorded by using a top objective through an analyzer. The optical images were captured by using a Canon SLR camera (model no: EOS 550D). All measurements were carried out under ambient conditions.

Optical Wave Guiding Studies. The optical wave guiding experiments were carried out using backscattering (reflected mode, B-LCOM) and transmission mode laser confocal optical microscope (T-LCOM) facility of the WiTec alpha 200 SNOM instrument. The Nd:YAG laser operating at 532 nm (maximum output power is 40 mW) was used for the excitation of the sheets (spot size ∼680 nm) and the bright- and dark-ield images were captured by using a color eyepiece video camera. In the backscattering mode experiment, a 100 × objective lens was used for the local excitation and for the collection of FL photons. The collected FL signal was sent to a CCD detector through a multimode optical fiber of diameter 25/125 μm (core/cladding). The FL spectrum was recorded using a 532 nm long pass edge filter (LPEF) and a 300 grooves/mm grating BLZ = 500 nm, with a 5 s integration time. Four accumulations were performed to acquire a single spectrum and the spectral resolution maximum was 0.1 nm. All measurements were carried out under ambient conditions.

To estimate the guided FL propagation efficiency at different positions, we used a T-LCOM setup. It consists of a bottom fix illumination stage, in which the illuminating source (laser) was fixed at the bottom of the piezo scanner and the laser light was point focused (∼5 μm spot size) on to a particular feature of the sample by using a 5× objective (see Scheme S1 in the Supporting Information). The FL light from the sample was collected through a top 100× objective (NA = 0.95). Light was focused at one of the edge of hexagonal nano-sheet by careful manual movement of the sample and also with fine screw adjustment of illuminating source. The efficiency of the guided light through the nano-sheet was calculated by scanning the entire area of a selected sheet with a top 100× objective. The signal was sent to a CCD counter through a 100/140 μm (core/cladding) diameter multimode optical fiber. The FL spectra from the sheets were obtained by focusing the top 100× objective at input and output points selectively. For the image scans in Figures 3 and 4, 80 × 64 data points with 0.5 s integration time were employed over the 20 μm × 16 μm scan area, whereas in the case of Figures 5 and 6, 108 × 80 data points with 0.5 s integration time were employed over the 27 μm × 20 μm scan area. After completion of the scan, the average spectrum was obtained from the image scan data profile. Finally, a particular FL peak of the the average spectrum was selected and used to generate three dimensional (3D) image using a Witec 2.08 software. This process involved baseline correction, background subtraction, and line integration of the selected peak. All measurements were carried out under ambient conditions.

3. RESULTS AND DISCUSSION

Hexagonal nanosheets were prepared as per our reported procedure.[17] The wine-red color sample solution containing dispersed nanosheets was drop-casted on a clean glass substrate and dried at room temperature for FESEM, AFM, and optical wave guiding studies. The nanosheets were nearly mono-disperse in nature (Figure 1a, g). The FESEM images showed eight facets of the hexagonal-shaped nanosheets (Figure 1a, b). TEM image exhibited bright contrast from the sheets, indicating its thin nature (Figure 1c). Additionally, a selected area electron diffraction (SAED) pattern showed bright diffraction spots representing the single-crystalline nature of the nano-sheets (Figure 1d). AFM studies on several monodispersed sheets showed that the thickness is in the

range of 110−180 nm (Figure 1e and Figures S1 and S2 in the Supporting Information). AFM topography and profile analyses of a typical hexagonal nano-sheet showed that the length (L) × width (W) × thickness (T) are in the range of ∼5.6 μm × ∼3.5 μm × ∼135 nm (Figure 1e, f). The solid state UV−vis absorption studies of the nanosheets showed absorbance features correspond to 431 nm soret B-band and four other Q-bands with a maxima at 520, 556, 595, and 653 nm (black line, Figure 1i). The solid-state emission studies displayed two FL emission bands at 653 and 719 nm (red line, Figure 1i). Laser confocal fluorescence microscope (LCFM) exhibited an intense red fluorescent from the nano-sheets upon excitation with 458 nm Ar+ laser (Figure 1g, h). Compound **1** readily crystallized into wine red color hexagonal block type single crystals in THF/H_2O. The single crystal XRD study revealed the monoclinic nature of the crystals with a $P21/n$ space group.[30] The solid state structure indicated that the primary driving force for the self-assembly process is weak inter molecular C−H···π (2.799 Å) interactions between the neighboring molecules (see Figure S3 in the Supporting Information).

For the light confinement studies, the nanosheets were deposited on a clean glass surface and studied using a laser confocal optical microscope (LCOM) setup equipped with a CCD detector. A 532 nm (Nd:YAG) laser was used as a point illumination source for electronic excitation of the building block molecules **1** and to generate strong red fluorescence at 653 and 719 nm from the nanosheet. At first, the experiment was performed using a B-LCOM facility to check the optical wave guiding behavior in a single nanosheet (Figure 2a). Localized laser (532 nm) excitation at the centre of a sheet showed generation of a strong red FL light and its propagation towards sheet edges (insets in Figure 2b, c). The spatially resolved FL spectrum of the nanosheet showed narrow optical
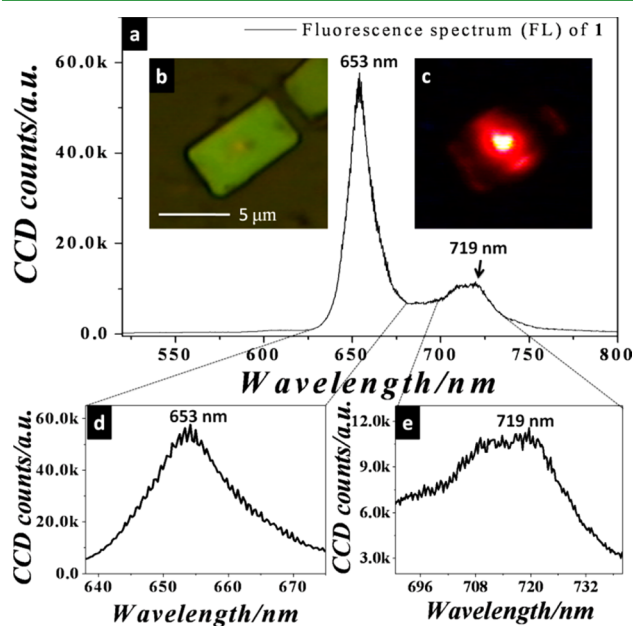

Figure 2. (a) Spatially resolved fluorescence spectrum (backscattered geometry) of a nanosheet obtained upon 532 nm laser excitation at the centre of a sheet. Inset show (b) bright-field image of a sheet and (c) dark field images of a sheet with a 532 nm LPEF. (d, e) Magnified regions of the 653 nm and 719 nm peak displaying optical modes.
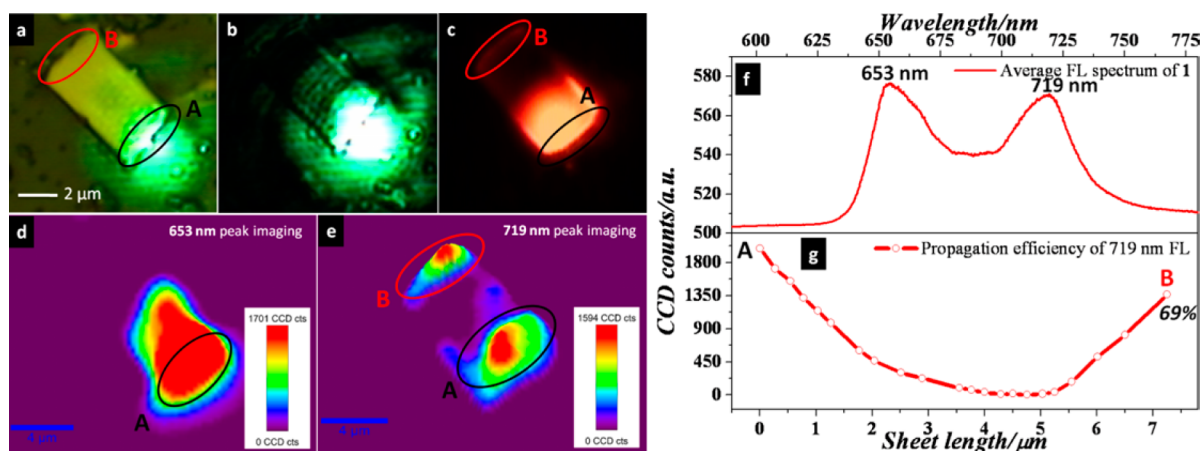
Figure 3. Interaction of a 532 nm laser beam at one of the short edges (A) of a single hexagonal sheet, (a) bright-field image, (b) dark-field image, (c) dark-field image with 532 nm LPEF displaying strong FL emission and its propagation towards the opposite edge (B). (d, e) 3D FL distribution maps of 653 and 719 nm bands, respectively. (f) Average FL spectrum of the single sheet used for the FL mapping. (g) Propagation efficiency plot of 719 nm FL in a single sheet. The black and red solid ellipsoidal circles denote the input and output points, respectively.
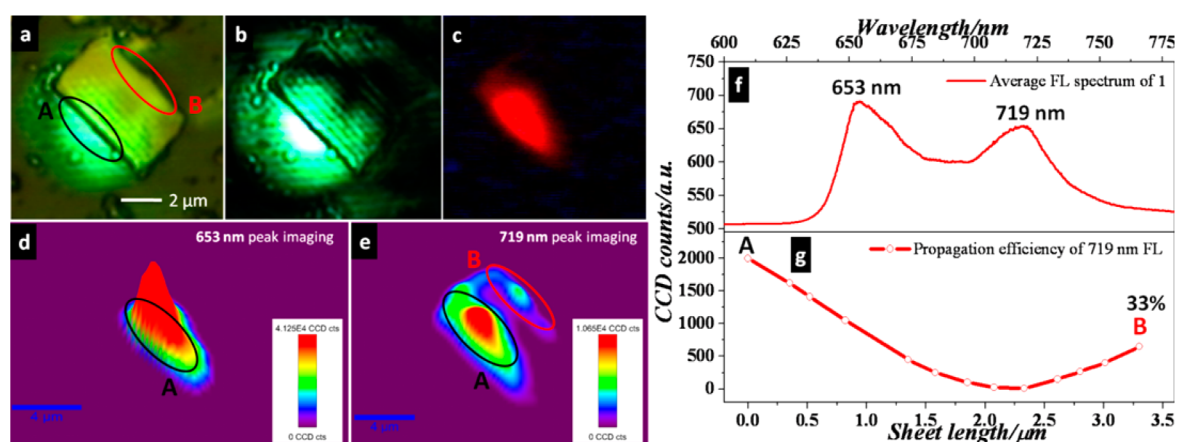

Figure 4. Interaction of a 532 nm laser beam at one of the longer edges (A) of a single sheet, (a) bright-field image, (b) dark-field image, (c) dark-field image with 532 nm LPEF displaying strong FL emission and it propagation towards opposite side (B). (d, e) 3D FL distribution maps of 653 and 719 nm bands, respectively. (f) Average FL spectrum of the single sheet used for the FL mapping. (g) Propagation efficiency plot of 719 nm FL in a single sheet. The black and red solid ellipsoidal circles denote the input and output points, respectively.

modes in the 653 and 719 nm FL peaks due to optical cavity effect (Figure 2d, e).

We have employed a T-LCOM facility to study the input light dependent FL propagation behaviour of sheets. When a 532 nm laser input beam was orthogonally point illuminated at one of the short edges of a sheet, at point A (Figure 3a), the dark-field images showed a weak light propagation to the opposite side, B (Figure 3b). We intended to probe the light propagation direction of the nanosheet by recording the distribution of FL light. Because the 532 nm excitation laser beam is in the forbidden Q-band absorption region of the molecular building block (see Figure 1i), the intensity of the FL light generation was weak and masked by the Rayleigh photons (laser). To clearly visualize the FL, we recorded the optical images using a color eye-piece video camera equipped with a 532 nm laser long pass edge filter (532 nm LPEF) to reject the most of the Rayleigh photons. Interestingly, the dark field images collected with a 532 nm LPEF clearly exemplify the presence of red FL light at the laser input point and its propagation to the opposite edge (at B) of the nanosheet (Figure 3c).

In addition, the 3D distribution images of FL photons were generated by collecting the average FL spectrum from the entire area of the sheet and by selectively mapping 653 and 719 nm "marker peaks" (Figure 3f). Comparison of individual 3D FL maps (Figure 3d,e) clearly showed the propagation of only 719 nm photons to the opposite end (B) of the sheet . The absence of 653 nm FL at point B is due to reabsorption of this particular wavelength by the molecular building block during propagation. This reabsorption is supported by solid state spectrum, as one can find a good overlap of emission and absorption bands at 653 nm (Figure 1i). A plot of 719 nm FL photons counts versus sheet length (ca. 7.22 μm) clearly showed 69% intensity at the output. This result demonstrated that the wave guiding nanosheets act as a wavelength filter by cutting-off a particular FL wave from propagation to the output through reabsorption. We verified this conclusion by performing similar experiments on a 25 μm longer sheet, which showed only 719 nm peak at B and complete disappearance of 653 nm photons (see Figure S4 in the Supporting Information). In addition, the spatially resolved spectra collected individually at positions A and B also showed optical modes indicating cavity effect.

Interestingly, the use of the same laser power to illuminate one of the longer sides of the same hexagonal sheet showed FL only at the input point A and no FL propagation to the opposite output end B. Upon increasing the laser input power by ca. 10× (see the CCD FL counts in Figure 4), a weak FL output was found at point B. The laser input and output positions are labeled as A and B in the bright field image and marked black and red circles, respectively (Figure 4a). The corresponding dark field image is shown in Figure 4b. In the presence of 532 nm LPEF, one can find a strong FL light at laser-sheet interaction point and a very weak FL at the corresponding opposite edges (Figure 4c). The 3D distribution maps of the 653 and 719 nm bands were obtained from the average spectrum (Figure 4f) displayed similar wavelength filtering effect (Figure 4d, e) as shown in Figure 3. The propagating efficiency of the 719 nm photons from *A* to sheet opposite edge B is ~33% (Figure 4g). Comparison of the results presented in Figures 3 and 4 clearly suggests the anisotropic nature of the nanosheets. This anisotropic wave guiding tendency is further supported by the polarization dependent wave transmission studies of nanosheets (see Figure S5 in the Supporting Information). Under cross-polarized position (see Figure S5b in the Supporting Information), nanosheets oriented in different angles exhibited different light intensities. For example, the horizontally and vertically oriented nanosheets looked completely darker, where as other intermediate orientation the nano-sheets are appeared brighter. The intensity variation is depends upon the nano-sheets orientation and was more pronounced at an angle ~45°. In fact, the solid state molecular packing along the crystallographic *c*-axis clearly suggested two different orientation of porphyrin rings (hence the dipoles) in the crystal lattice (see Figure S3 in the Supporting Information).

To study the evanescent coupling between two nano-sheet waveguides in close contact at a distance (*d*), i.e., $d \lesssim \lambda$, two sheets arranged in head-to-tail manner was identified. In the bright-field image, the black, dotted red, and red circles represent the laser input (A), junction between two sheets (B), and final output point (C), respectively (Figure 5a). The corresponding dark-field image is shown in Figure 5b. In the presence of 532 nm LPEF, the dark-field image showed intense FL at the input point (A), junction (B), and opposite exit (C). Here at junction B, the output of sheet-1 acts as an input to sheet-2. Figure 5c imaged with a LPEF clearly showed a variation in the FL intensity at points A, B, and C. The corresponding 3D FL (653 and 719 nm) distribution maps genetrated from the averaged FL spectrum are shown in images d and e in Figure 5. As observed in previous cases, the 653 nm FL light was only found at the input point A, whereas the 719 nm FL band was found at A, B, and C. The FL efficiency in this sheet arrangement was estimated by integrating the intensity of the photons at the output signal as a function of position and dividing the output light by the input light. The efficiency profile reveal the propagation of 719 nm FL from one sheet to another (B/A = 12% and C/B = 56%) through evanescent coupling (Figure 5f). The calculated efficiency of the two sheets arranged in head-to-tail manner (Figure 5), clearly demonstrated a dramatic reduction of the output at junction B (12%) due to the continuous propagation of FL light from sheet-1 to -2 through efficient optical coupling between the sheets. Considering the optical loss at the coupling point B, the final output at C (56%) is nearly akin to the single-sheet output (69%).
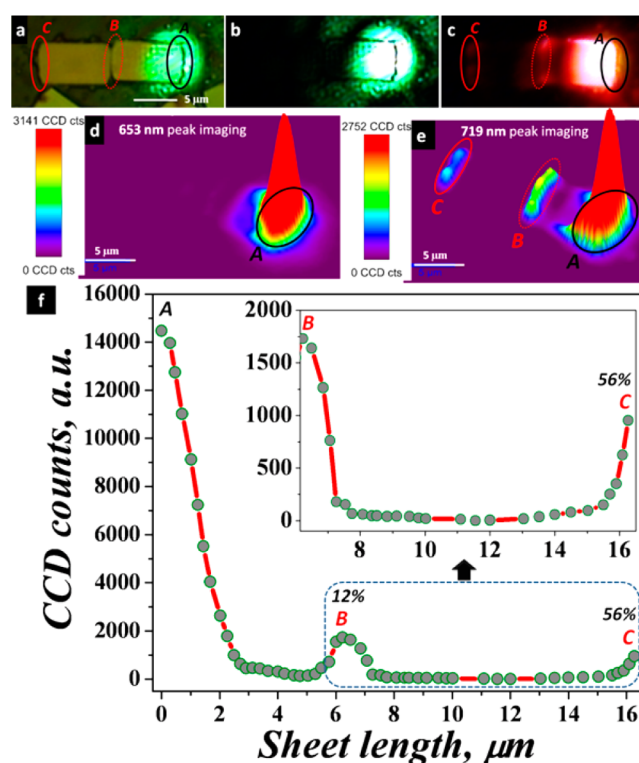

Figure 5. Interaction of 532 nm laser with the one of short edge (A) of a two hexagonal sheets arranged in a head-to-tail fashion. (a) Bright-field image, (b) dark-field image without 532 nm LPEF, (c) dark-field image with 532 nm LPEF displaying strong FL emission and its propagation towards opposite edge. (d, e) Corresponding 653 and 719 nm peak 3D mapping images. (f) Intersheet propagation efficiency profile of 719 nm FL is shown as a plot of 719 nm intensity versus sheet length at points A−C corresponding to image e. The black and red ellipsoidal circles denote the input and output points, respectively. The dotted red circle is the junction B between two sheets.

Similarly, optical coupling between two sheets arranged in a side-to-side geometry was investigated (Figure 6a). The input point, junction, and opposite exit are marked as A, B, and C (Figure 6b). As observed in previous results presented in Figure 4, only at high laser power (see the CCD FL counts, Figure 6e, f) was a weak propagation of light to the opposite edges of side-to-side sheets observed. The corresponding dark-field image is shown in Figure 6c. The dark-field image in presence of 532 nm LPEF showed a weak FL light coupling between the sheets (Figure 6d). The 3D FL distribution maps of 653 and 719 nm bands showed only 719 nm FL band at C (Figure 6f) and complete reabsorbance of 653 nm band (Figure 6d). The efficiency profile of 719 nm FL band as a function of sheet length (ca. 8.4 μm) exhibited an optical output of ~29% (B/A, Figure 6g). As mentioned above, in this geometry, a decrease in output intensity is attributed to a weak output of sheet-1 at junction B and subsequent cut down of output intensity at C.

4. CONCLUSIONS

In summary, we examined for the first time, FL wave guiding behavior of nearly hexagonal 2D *meso*-tetratolylphorphyrin nano-sheets (thickness range ~110−180 nm). The nanosheets emit FL bands at 719 and 653 nm upon local excitation and display optical modes due to cavity effect. Interestingly, the 653 nm FL photon intensity drastically drops during propagation because of reabsorption as its travel path length along the
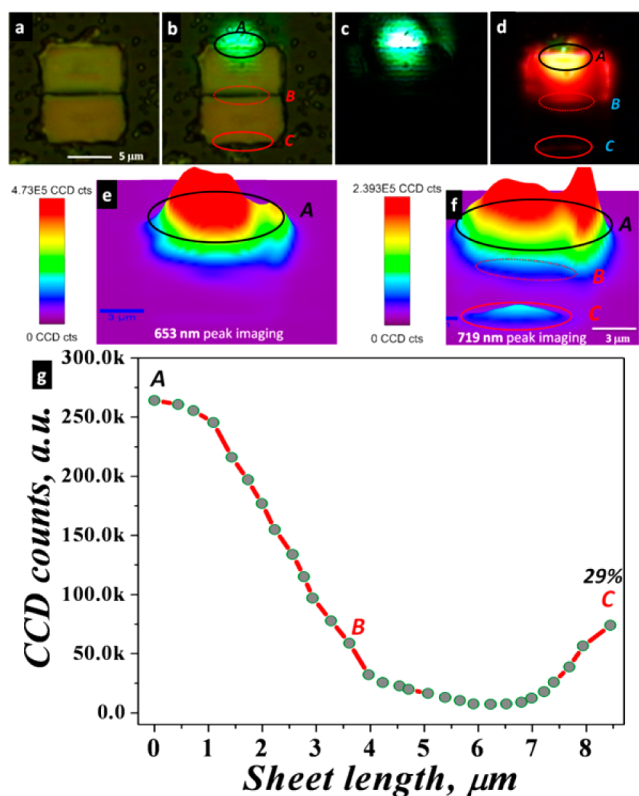
Figure 6. Interaction of 532 nm laser with the one of the long edge (A) of a two hexagonal sheets arranged in a side-to-side fashion. (a, b) Bright-field image, (c) dark-field image without 532 nm LPEF, (d) dark field image with 532 nm LPEF displaying strong FL emission and its propagation towards opposite edge. (e, f) Corresponding 653 and 719 nm peak 3D mapping images. (g) Intersheet propagation efficiency profile of 719 nm FL is shown as a plot of 719 nm intensity versus sheet length at points A–C corresponding to image f. The black and red ellipsoidal circles denote the input and output points, respectively. The dotted red circle is the junction B between two sheets.

nanosheet increases. Hence, these nanosheets act as wavelength filter and transmit only one type of FL photons (719 nm) to the output, although two FL bands (719 and 653 nm) were generated at the input. The FL wave guiding behavior was also dependent on the input light position due to anisotropic nature of nanosheets. Additionally, intersheet optical wave propagation efficiency through evanescent coupling between two sheets arranged in different geometries has also been demonstrated.

■ ASSOCIATED CONTENT

Ⓢ Supporting Information

Noncontact mode AFM histogram profile of several hexagonal nanosheets, solid-state packing diagram of **1** (CCDC 960056), images of 25 μm long sheet acting as wavelength filter and optical light anisotropic character of nanosheets (Figures S1–S5). Schematic diagram of the optical wave guiding experimental setup is shown in Scheme S1 and table of crystal data and structure refinement parameters described in Table S1. This material is available free of charge via the Internet at http://pubs.acs.org.

■ AUTHOR INFORMATION

Corresponding Author
*Tel: (+)91-40-2313-4824. E-mail: rcsc@uohyd.ernet.in or chandrasekar100@yahoo.com.

Author Contributions
The manuscript was written through contributions of all authors. All authors have given approval to the final version of the manuscript.

Notes
The authors declare no competing financial interest.

■ ABBREVIATIONS

EP, exciton polariton
FL, fluorescence
SEM, scanning electron microscopy
TEM, transmission electron microscopy
LCOM, laser confocal optical microscopy
AFM, atomic force microscopy
PLOM, polarized light optical microscopy
LPEF, long pass edge filter
CCD, charge coupled device

■ REFERENCES

(1) Yanagi, H.; Morikawa, T. *Appl. Phys. Lett.* **1999**, *75*, 187−189.
(2) Zhao, Y. S.; Fu, H.; Peng, A.; Ma, Y.; Liao, Q.; Yao, J. *Acc. Chem. Res.* **2010**, *43*, 409−418.
(3) Zhang, C.; Zhao, Y. S.; Yao, J. *Phys. Chem. Chem. Phys.* **2011**, *13*, 9060−9073.
(4) Zhao, Y. S.; Fu, H.; Peng, A.; Ma, Y.; Xiao, D.; Yao, J. *Adv. Mater.* **2008**, *20*, 2859−2876.
(5) Balzer, F.; Bordo, V. G.; Simonsen, A. C.; Rubahn, H.-G. *Phys. Rev. B* **2003**, *67*, 115408−115415.
(6) Takazawa, K.; Kitahama, Y.; Kimura, Y.; Kido, G. *Nano Lett.* **2005**, *5*, 1293−1296.
(7) Zhao, Y. S.; Xu, J. J.; Peng, A. D.; Fu, H. B.; Ma, Y.; Jiang, L.; Yao, J. *Angew. Chem. Int. Ed.* **2008**, *47*, 7301−7305.
(8) Balzer, F.; Bordo, V. G.; Simonsen, A. C.; Rubahn, H. -G. *Appl. Phys. Lett.* **2003**, *82*, 10−12.
(9) Schiek, M.; Balzer, F.; Al-Shamer, K.; Brewer, J. R.; Lutzen, A.; Rubahn, H.-G. *Small* **2008**, *4*, 176−181.
(10) Zhao, Y. S.; Xu, J. J.; Peng, A. D.; Fu, H. B.; Ma, Y.; Jiang, L.; Yao, J. *Angew. Chem., Int. Ed.* **2008**, *47*, 7301−7305.
(11) Zhao, Y. S.; Fu, H. B.; Peng, A. D.; Ma, Y.; Xiao, D. B.; Yao, J. *Adv. Mater.* **2008**, *20*, 2859−2876.
(12) Zhang, C.; Zou, C. L.; Yan, Y. L.; Hao, R.; Sun, F. W.; Han, Z. F.; Zhao, Y. S.; Yao, J. *J. Am. Chem. Soc.* **2011**, *133*, 7276−7279.
(13) Kim, F. S.; Ren, G. Q.; Jenekhe, S. A. *Chem. Mater.* **2011**, *23*, 682−732.
(14) Yao, W.; Yan, Y.; Xue, L.; Zhang, C.; Li, G.; Zheng, Q. D.; Zhao, Y. S.; Jiang, H.; Yao, J. N. *Angew. Chem., Int. Ed.* **2013**, *52*, 8713−8717.
(15) Chandrasekhar, N.; Chandrasekar, R. *Chem. Commun.* **2010**, *46*, 2915−2917.
(16) Chandrasekhar, N.; Chandrasekar, R. *Angew. Chem., Int. Ed.* **2012**, *51*, 3556−3561; *Angew. Chem.* **2012**, *124*, 3616−3621.
(17) Chandrasekhar, N.; Mohiddon, Md. A.; Chandrasekar, R. *Adv. Opt. Mater.* **2013**, *1*, 305−311.

(18) Hui, P.; Chandrasekar, R. *Adv. Mater.* **2013**, *25*, 2963−2967.

(19) Basak, S.; Chandrasekar, R. *J. Mater. Chem. C* **2013**, DOI: 10.1039/C3TC31576B.

(20) Chandrasekar, R. *Phys. Chem. Chem. Phys.* **2014**, DOI: 10.1039/C3CP54994A.

(21) Ulbrich, R. G.; Fehrenbach, G. W. *Phys. Rev. Lett.* **1979**, *43*, 963−966.

(22) Chu, S.; Wong, S. *Phys. Rev. Lett.* **1979**, *48*, 738−741.

(23) Andreani, L. C.; Panzarini, G.; Gerard, J. M. *Phys. Rev. B* **1999**, *60*, 13276−13279.

(24) Takazawa, K.; Inoue, J. -I.; Mitsuishi, K.; Takamasu, T. *Adv. Mater.* **2011**, *23*, 3659−3663.

(25) Takazawa, K.; Inoue, J. -I.; Mitsuishi, K. *ACS Appl. Mater. Interfaces* **2013**, *5*, 6182−6188.

(26) Takazawa, K.; Inoue, J. −I.; Mitsuishi, K.; Kuroda, T. *Adv. Funct. Mater.* **2013**, *23*, 839−845.

(27) van Vugt, L. K.; Rühle, S.; Ravindran, P.; Gerritsen, H. C.; Kuipers, L.; Vanmaekelbergh, D. *Phys. Rev. Lett.* **2006**, *97*, 147401−147404.

(28) van Vugt, L. K.; Piccione, B.; Agarwal, R. *Appl. Phys. Lett.* **2010**, *97*, 061115.

(29) Medforth, C. J.; Wang, Z.; Martin, K. E.; Song, Y.; Jacobsen, J. L.; Shelnutt, J. A. *Chem. Commun* **2009**, 7261−7277.

(30) Butcher, R. J.; Jameson, G. B.; Storm, C. B. *J. Am. Chem. Soc.* **1985**, *107*, 2978−2980.